A computational and experimental investigation of the anchoring of organosilanes on the halloysite silicic surface

Lorenzo Lisuzzo[a], Marco Bertini[a], Giuseppe Lazzara[a], Chiara Ferlito[a], Francesco Ferrante[a,*], Dario Duca[a]

[a] *Dipartimento di Fisica e Chimica "E. Segrè", Università degli Studi di Palermo, Viale delle Scienze - 90128 Palermo, Italy*

Abstract

In this work, the effect of halloysite nanotubes alkali activation on its grafting efficiency with organosilanes was studied by Density Functional Theory and experimental investigations. In particular, computational analysis allowed to enlight the structural properties of the organic molecules attached to the silanol groups on halloysite outer surface, The energetics of the reactions showed that the pretreatment with a base is crucial for the modification of the surface due to the appearance of a high number of active sites which led to thermodynamically favored exothermic processes. Experimental evidences were in good agreement with calculation hypothesis. For instance, the coating efficiency is higher after the alkali activation of the inorganic counterpart for both the investigated organosilanes. The findings here reported are important in order to improve any functionalization protocols for aluminosilicates without variations or loss of the hollow nanotubular morphological features and it paves the ground to halloysite based technological applications in many fields, from nanotechnology to catalysis.

Keywords: Halloysite nanotubes, Functionalization, Siloxanes, Heterogenous catalysis

*Corresponding author

1. Introduction

Clay minerals attract the interest of the scientific community due to their peculiar properties, which make them good platforms for the design of functional inorganic or hybrid materials to be exploited in many technological applications. Among clays, Halloysite Nanotubes (Hal) hold a certain importance as a result of both their surface chemistry and morphological features (Lvov et al., 2016). Hal are natural occurring 1:1 aluminum phyllosilicates with $Al_2Si_2O_5(OH)_4 \cdot nH_2O$ as stoichiometric formula, where n can be 0 or 2 and it corresponds to the number of water molecules in the interlayer space, thus resulting in either the dehydrated 7Å-halloysite or in the hydrated 10Å-halloysite, respectively (Zsirka et al., 2017; Makó et al., 2020). Being structurally composed by the alternation of a tetrahedral Si−O based sheet which is overlapped to an octahedral Al−OH sheet, halloysite displays different groups in the external and internal surfaces (Hua et al., 2023; Ferrante et al., 2017). In particular, the kaolinite-like sheet rolls up, thus providing the nanoclay with its most distinctive property, i.e. its hollow nanotubular shape (Zhang et al., 2019a; Liu et al., 2016). As a result, the external silicon based surface is negatively charged and the inner aluminum based surface is positively charged in the pH range from 2 to 8 (Vergaro et al., 2012). Since it is extracted from natural deposits in different geographical areas, the dimensions of halloysite nanoparticles can be different (Lisuzzo et al., 2022). The length may vary from the submicron scale to 2-3 µm, the outer diameter from 15 to 200 nm wheares the inner diameter can range from 10 to 100 nm (Pasbakhsh et al., 2013; Liu et al., 2021).

Several studies report about the biocompatibily and lack of cytotoxicity of halloysite nanotubes. (Rozhina et al., 2021; Kryuchkova et al., 2016) These aspects, together with the high specific surface area, eco-compatibily, abundant availability and low cost, are essential to burst their use in industrial domains. For instance, Hal have been widely investigated as inorganic fillers for nanocomposites manufacturing, showing their effect in improving thermal and mechanical properties of, among others, bioplastics and nanopapers (Lisuzzo et al.,

2020a). Also, they found application in food packaging, environmental remediation, building science, drug delivery, cultural heritage treatment and catalysis (Sadjadi et al., 2017; Sidorenko et al., 2018, 2021; Spepi et al., 2016; Liu et al., 2019; Panchal et al., 2020; Haw et al., 2020). Nonetheless, there are some issues to handle and to overcome before using Hal and exploiting their full potential. Halloysite does not display a long term colloidal stability, as the nanotubes tend to aggregate and settle at the bottom of aqueous dispersions, being the sedimentation driven by the high density of the nanoparticles (Lisuzzo et al., 2019). However, reaching a good stability is imperative for every application of halloysite, especially in liquid media, and it is needed as first condition in the synthetic protocol for the preparation of new materials. In this scenario, the chemical functionalization of halloysite surfaces showed to play a major role. Indeed, the inner positive surface can be functionalized with negative molecules, whereas the outer negative surface can be modified with positive species (e.g. polymers, surfactants, biopolymers) by electrostatic interactions (Zhang et al., 2019b). Moreover, the surface modification can also be conducted by chemical covalent grafting with organosilanes (Mehdizadeh et al., 2022). As a matter of fact, the functionalization of clays with silanes is important for polymer-clay nanocomposites, since it enhances the dispersion of the solid nanoparticles in the polymeric matrix thus improving the mechanical properties of the resuling materials. Literature reports about the grafting of halloysite inner surface, which bears hydroxyl groups (aluminols), with organosilanes and about the effects of thermal and evacuation pretreatments, where the former is carried out to remove physically adsorbed water and to improve the grafting efficiency (Yuan et al., 2008a). However, the silanization of the external surface is still an open issue because it consists of siloxane ($Si-O-Si$) groups with just few $Si-OH$ groups at the edges of the nanotubes or in some defects (Ferrante et al., 2015). Undoubtedly, the presence of hydroxyl groups is the necessary condition to conduct any covalent modification. In order to improve the functionalization efficiency, halloysite nanotubes are very often pretreated or alkali activated (Wang et al., 2013; Shankar et al., 2018; De Silva et al., 2015).

In our previous work, we conducted computational and experimental investigations to enlighten the mechanisms of silanol groups formation on the outer silicic surface of Hal as products of the reactions in alkaline aqueous dispersions (Ferrante et al., 2023). Herein, it was found that the creation of different arrays of Si−OH groups is a highly exotermic process in the presence of sodium hydroxyde and the final activated nanotubes did not change their morphological features, despite the increased number of active sites. Being the silanization of the outer surface important in many technological applications, from the delivery of biologically active species (Liu et al., 2016; Massaro et al., 2022), to the removal of pollutants from aqueous solutions (Cataldo et al., 2018; Zhu et al., 2017), to the immobilization of metal nanoparticles for catalysis (Sadjadi & Atai, 2018), its optimization and deep understanding are crucial. The present work is aimed at investigating the role of alkaline activation on the efficiency of silanes grafting on halloysite silicon-based surface. The formation of Si−OH groups and their reactions with organosilanes, namely the (3-aminopropyl)triethoxysilane (APTES) and the N-3-(trimethoxysilyl)propyl ethylenediamine (AEAPTMS; see Figure 1), will be focused by a density functional theory based computational approach and the results will be corroborated by experimental analysis to provide meaningful insights about the effects of chemical activation and about the grafting mechanism and efficiency. It should be noted that, among the different applications, the silanization of halloysite outer surface is a challenge for industrial and catalytic purposes. The termination of the silane chain can bear different atoms, each one with a peculiar affinity towards metal particles. This factor, together with halloysite hollow nanotubular proper morphology, can lead to the design of multicatalytic system with different active sites in isolated environments, each one catalyzing a specific reaction or process.

2. Models and Computation Details

All the calculations in this work were carried out by using the Gaussian 16 software (Frisch et al., 2016). The geometries of halloysite functionalized struc-

tures were optimized within the Density Functional Theory (DFT) framework, by using the M06-L exchange-correlation functional (Zhao & Truhlar, 2006) together with the resolution of identity approximation (Eichkorn et al., 1997), in order to reduce the computational cost for investigating systems with large dimensions. The SVP valence double-zeta plus polarization basis set of Ahlrichs and co-workers (Schaefer et al., 1992) was employed and the corresponding auxiliary functions needed for RI approximation were generated at run time. A cluster approach was used throughout the whole investigation. The starting pristine halloysite surface was tailored from a nanotube model built and investigated through a Density Functional Tight Binding approach (Ferrante et al., 2015, 2017). Herein, all the oxygen atoms placed at the cutting edges were kept frozen in their positions during geometry optimization, thus maintaining the surface curvature. Aimed at investigating the functionalization of halloysite surface with organosilanes, APTES and AEAPTMS were considered and their attachments to the clay surface were investigated by exploiting their most stable conformations obtained in vacuum conditions. In particular, in the optimized geometry of APTES the alkyl chain is bent as a result of very weak interactions between the nitrogen atom and the methylenic hydrogen, while the geometry of the alkyl chain in AEAPTMS is ruled by the intramolecular NH···N hydrogen bond. For what concerns halloysite, the Hal−Si$(2,1)^{-}$, the Hal−Si$(4,2)^{2-}$, the Hal−Si$(6,3)^{3-}$ and the Hal−Si−$v_1{}^{-}$ structures taken from (Ferrante et al., 2023) represent the starting points for the simulated functionalization reactions. The resulting modified structures will be labeled as Hal-S^{x}A^y, where S indicates the silicic surface and A = APTES or AEAPTMS; x is the number of silanol groups on the starting surface model (or x = v for the system derived from Hal−Si−$v_1{}^{-}$, having a silicon vacancy) and y is the number of −OR groups (R = Et or Me) left on A after the functionalization.

[Figure 1 about here.]

3. Materials and Methods

3.1. Materials

Halloysite (specific surface area of 65 $m^2\,g^{-1}$ and specific gravity of 2.53 $g\,cm^{-3}$), (3-Aminopropyl)triethoxysilane (APTES, $H_2N(CH_2)_3Si(OC_2H_5)_3$, 99%), N-3-(trimethoxysilyl)propyl ethylenediamine (AEAPTMS, $(CH_3O)_3Si(CH_2)_3NHCH_2CH_2NH_2$, 97%), sodium hydroxide (≥97.0%) and toluene (anhydrous, 99.8%) were purchased from Sigma-Aldrich and used without any further purification. Absolute ethanol (≥99.8%) is a Honeywell product.

3.2. Alkaline modification of Halloysite

The alkaline activation of halloysite was carried out as reported in literature (Ferrante et al., 2023). Briefly, a dispersion containing 2 g of the nanoclay in 40 cm^3 of NaOH 4M was prepared and kept under stirring for 30 minutes at 80 °C, before being separated by centrifugation (5000 rpm, 10 min), washed and dried overnight at 60 °C. The sample will be referred to as alkaline Hal (aHal).

3.3. APTES functionalization of Halloysite

Grafting of Hal outer surface with γ-Aminopropyltriethoxysilane was conducted as described in literature by Yuan et al. (Yuan et al., 2008a). Briefly, 0.6 g of the clay was added to a solution composed of 2 cm^3 APTES in 25 cm^3 of toluene. The dispersion was sonicated for 30 min and refluxed for 20 h at 120 °C under constant stirring. The organosilane functionalized clay was separated by centrifugation and washed six times with toluene before being dried overnight. Both pristine and alkaline halloysite were functionalized according to this procedure, resulting in the Hal-APTES and aHal-APTES samples.

3.4. AEAPTMS functionalization of Halloysite

Grafting of Hal outer surface with N-3-(trimethoxysilyl)propyl ethylenediamine was performed using a procedure similar to that reported in literature by Takahara et al. (Takahara et al., 2005). In particular, 0.5 g of the clay was added to 50 cm^3 of solution containing AEAPTMS 0.4 M in toluene. The

dispersion was sonicated and magnetically stirred for 16 h at room temperature. The aminoalkylated clay was separated by centrifugation and washed with ethanol before being dried for 4 h. Both pristine and alkaline halloysite were functionalized according to this procedure, resulting in the Hal-AEAPTMS and aHal-AEAPTMS samples.

3.5. Experimental analysis

Thermogravimetry (TGA) was conducted by using a Q5000 IR (TA Instruments) apparatus operating with N_2 flow at 25 $cm^3\,min^{-1}$ for the sample and 10 $cm^3\,min^{-1}$ for the balance, respectively. The investigated temperature range was set from room temperature to 800 °C, the heating rate was 20 °C min^{-1}. The calibration was previously carried out on the basis of the Curie temperatures of standards (Blanco et al., 147-153). Fourier transform infrared investigation was performed through a Frontier FTIR spectrometer (PerkinElmer), working at room temperature using 64 scans in the range between 4000 and 500 cm^{-1} with 2 cm^{-1} spectral resolution. The experiments were conducted on KBr pellets with an amount of milled sample <2 wt%. X-ray Fluorescence (XRF) Spectrometry was carried on by means of an Olympus Innov X DS-2000 Delta Standard Alloy XRF Handheld Analyzer operating in the Alloy Plus analysis mode. The X-Ray Diffraction (XRD) analysis was conducted through a Rigaku (MiniFlex) diffractometer based on a copper Kα radiation source including a nickel filter. The patterns were recorded in the range 2-70° with a rate of 20 ° min^{-1} and a step of 0.02°. The voltage was 40 kV and the current 15 mA.

4. Results and Discussion

4.1. Halloysite functionalization DFT analysis

All the investigated functionalization processes are collected in Table 1, together with the corresponding global reaction energies taken by starting from the pristine halloysite model as reactant. The partial reaction energies corresponding to the attachment of APTES and AEAPTMS on the functionalized

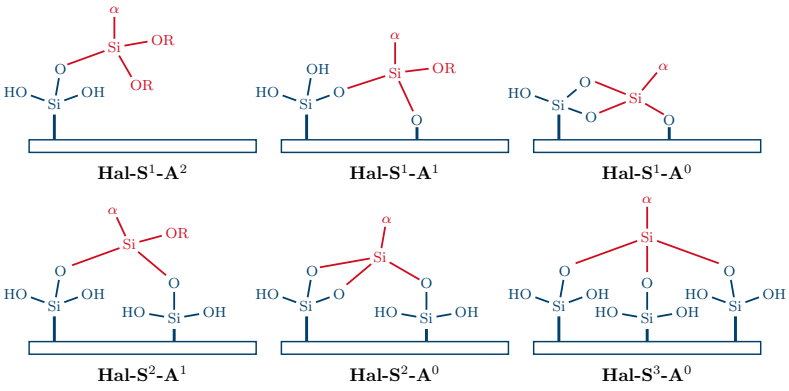

Scheme 1: Pictorial representation of the six Hal−$S^{m}A^{3-n}$ systems (m, n = 1, 2, 3) derived by functionalization of the Hal model bearing silanol groups protruding from the silicic surface. The blue atomic centers belong to the Hal silicic surface, which is represented by the rectangle; the parts in red color are the fragments of APTES ($\alpha = (CH_2)_3NH_2$, R = CH_2CH_3) or AEAPTMS ($\alpha = (CH_2)_3NH(CH_2)_2NH_2$, R = CH_3) remaining after the functionalization.

halloysite models, instead, are reported in Table 2. A look at these tables reveals that the differences, in term of reaction energies, between APTES and AEAPTMS functionalizations are not relevant, so that in the following a unified discussion can be reported. Scheme 1 shows the conceptualization of the 6 Hal-S^{x}-A^{y} systems, whose structural and energetic properties will be detailed in the following.

[Table 1 about here.]

[Table 2 about here.]

The alkaline activation of halloysite surface after treatment with a strong base was investigated in our previous study. Herein, it is reported about the formation of Hal−$Si(n,m)^{m-}$ systems and the appearance of surface silanol groups through the reaction of halloysite with water and hydroxide ions in the ratio

1:n:m (Ferrante et al., 2023). In particular, the following reaction:

$$\mathrm{Hal} + 2\,\mathrm{H_2O} + \mathrm{OH^-} \longrightarrow \mathrm{Hal{-}Si(2,1)^-} \tag{1}$$

resulted in the formation of a structure, which consisted of a $\mathrm{Si(OH)_3}$ group protruding from the external surface of the clay, two SiOH moieties on the silicic array and a negative charge on an interlayer oxygen center. Its formation occurred with an energy release of ca. 700 $\mathrm{kJ\,mol^{-1}}$ and, as a consequence, it was strongly favored from the thermodynamic point of view. As a matter of fact, the appearance of silanol groups on Hal silicic surface is crucial since they represent the anchor points for the attachment of the organosilanes in the functionalization reactions. The processes that were investigated at first are the following ones:

$$\mathrm{Hal{-}Si(2,1)^- + A} \longrightarrow \mathrm{Hal{-}S^1A^2 + ROH} \tag{2}$$

$$\mathrm{Hal{-}Si(2,1)^- + A} \longrightarrow \mathrm{Hal{-}S^1A^1 + 2\,ROH} \tag{3}$$

$$\mathrm{Hal{-}Si(2,1)^- + A} \longrightarrow \mathrm{Hal{-}S^1A^0 + 3\,ROH} \tag{4}$$

The optimized structures of functionalized Hal produced by the reaction (2) above are reported in Figure 2. It shoud be noted that from the structural point of view there are no sensible differences between the outcomes of APTES or AEAPTMS functionalizations: both geometries show the formation of a hydrogen bond between the OH from the surface and the OR moiety from the organosilane. Further, in both cases the N-alkil chain is elongated perpendicularly to the silicic surface. Reaction (2) occurs with the release of only 31 $\mathrm{kJ\,mol^{-1}}$ (Table 2), but it becomes largely exothermic (Table 1) if coupled with reaction (1). The product of process (3) forms after two hydrolysis reactions involving one Si-OH from the silanol group and the OH moiety left on the surface after the $\mathrm{Hal{-}Si(2,1)^-}$ formation, with a global release of energy slightly higher than the one calculated for reaction (4). In the optimized geometry of the $\mathrm{Hal{-}S^1A^1}$ system, showed in Figure S1 and S2 of Supporting Information the two other groups bonded to the silicon center of APTES are forced to lie almost parallel to the silicic surface; this is true also for the first part

of the $-(CH_2)_3NH(CH_2)NH_2$ chain in AEAPTMS, while the second fragment stretches upwards. A sort of destabilization effect in Hal$-S^1A^1$ is likely due to deformation of the bonding configuration occurring between the A fragment and the protruding silanol; in fact, all the configuration tension seems to be located on the latter, being this group more mobile than the surface hydroxyl, and the results are a sensibly wider Si$-$O$-$Si angle (increased by 15°) and longer Si$-$O bond (by ca. 0.05 Å) with respect to the corresponding configuration in Hal$-S^1A^2$. In process (4) two OH groups from the raised $Si(OH)_3$ tetrahedron and one OH group from the OH moiety are the active sites for the nucleophilic attack on the silicon center, with the resulting Hal$-S^1A^0$ system showing no OR group left on A. In this case the functionalization with both the organosilanes is a highly endothermic process, as it needs an energy of ca. 190 kJ mol^{-1} to occur. This effect can be most likely related to the poor availability of active Si$-$OH sites on the surface, necessarily leading to the formation of a system showing an innatural Si$-$O$-$Si$-$O ring, which provides ring tension to the final optimized structures (see Figure S3 and S4 of Supporting Information). Taking into account the exothermicity of Hal$-$Si(2,1)$^-$ formation (Ferrante et al., 2023), the global reaction energies calculated starting from pristine halloysite are -509.4 and -507.9 kJ mol^{-1}, but it is clear that this situation is not a likely one: when the Hal surface is sparsely populated by silanol groups the functionalization would occur through many partial hydrolysis processes on a large number of sites instead of total hydrolisys on few sites.

[Figure 2 about here.]

A step forward is moved by investigating the functionalization of the Hal$-$Si(4,2)$^{2-}$ structure, which is the result of the following reaction:

$$\text{Hal} + 4\,H_2O + 2\,OH^- \longrightarrow \text{Hal}-\text{Si(4,2)}^{2-} \qquad (5)$$

which shows two $Si(OH)_3$ groups protruding from the surface of the halloysite model, four Si(OH) groups embedded in the silicic array and two negative charges as a consequence of the alkaline treatment. In this case, the com-

putational study was focused on the energetic of the following processes:

$$\mathrm{Hal{-}Si(4,2)}^{\,2-} + \mathrm{A} \longrightarrow \mathrm{Hal{-}S^2A^1} + 2\,\mathrm{ROH} \tag{6}$$

$$\mathrm{Hal{-}Si(4,2)}^{\,2-} + \mathrm{A} \longrightarrow \mathrm{Hal{-}S^2A^0} + 3\,\mathrm{ROH} \tag{7}$$

The optimized structures of the products of reaction 6, with A = APTES and AEAPTMS, are reported in Figure 3. In these structure a network of hydrogen bonds exists also after the functionalizations, involving the surface and the silanolic OH groups. The geometry of the surface anchoring sites, along with the position of OR moiety, make the N-alkyl chain to tilt sensibly with respect to the surface normal. The reaction step 6 shows only low exothermicity, which obviuosly is more than compensated by the energy release characterizing reaction 5, making the global process to show an exothermicity larger than 1100 $\mathrm{kJ\,mol^{-1}}$. The fact that this value is well below than the double of the energy released by the combined 1 and 2 processes is due to the issue, already hypothesized in (Ferrante et al., 2023), regarding the energetic preference toward the presence of silanol groups sparse on the Hal surface with respect to the formation of clustered configurations, a situation, this last, that would occur at extreme alkaline conditions.

[Figure 3 about here.]

Bearing the surface of $\mathrm{Hal{-}Si(4,2)}^{\,2-}$ two tetrahedra, there is no room for interactions with surface OH groups, so the nucleophilic attack on the Si center of the silanes is conducted by two OH groups from one $\mathrm{Si(OH)_3}$ and one OH group from a second $\mathrm{Si(OH)_3}$. As happened in the case of $\mathrm{Hal{-}S^1A^0}$ formation, the presence of a tensioned Si−O−Si−O ring in the $\mathrm{Hal{-}S^2A^0}$ product (see Figure S5 and S6 of Supporting Information) makes reaction (7) highly endothermic, both for the APTES and AEAPTMS functionalizations. Nevertheless, the loss in exothermicity in this case, when reactions (6) and (7) are compared and global reaction energies are considered, is equal to 160 $\mathrm{kJ\,mol^{-1}}$ in the average, while the same quantity was equal to ca. 210 $\mathrm{kJ\,mol^{-1}}$ for the corresponding processes occurring in the $\mathrm{Hal{-}Si(2,1)}^{\,-}$ ancestor, represented by

equations (2)-(4). This can be considered another hint that a larger availability of active Si-OH sites on the Hal surface is beneficial to the functionalization reactions.

In order to have more insights about the effect of the alkaline pretreatment on the efficiency of functionalization, we carried out further computational studies by considering a third structure, namely Hal−Si(6,3)$^{3-}$, produced by the reaction:

$$\mathrm{Hal} + 6\,\mathrm{H_2O} + 3\,\mathrm{OH^-} \longrightarrow \mathrm{Hal{-}Si(6,3)}^{3-} \tag{8}$$

It shows three $\mathrm{Si(OH)_3}$ tetrahedra protruding from the surface of halloysite, three negative charges and high configuration flexibility as a consequence of the alkaline treatment. In this case, the computational study was focused on the following process:

$$\mathrm{Hal{-}Si(6,3)}^{3-} + \mathrm{A} \longrightarrow \mathrm{Hal{-}S^3A^0} + 3\,\mathrm{ROH} \tag{9}$$

Here, the nucleophilic attack on the Si center of the silanes is conducted by three OH, each one of them coming from one of the three different tethaedra raised above the halloysite surface. The optimized structures are reported in Figure 4. It was found that the best geometrical arrangement for the anchoring portion in this system is not a symmetrical one, as one could imagine by mentally drawing the Si atom of the functionalizing organosilane at the center of a triangle whose vertex are occupied by the silanol groups of the surface. As a matter of fact, the optimized geometry of the portion above can be viewed as originated by two almost equivalent silanol groups plus a third group which adjusts its position driven by forces which, other than the main geometric constraints, include the formation of hydrogen bond between the silanols, the asymmetry of the underneath surface and even by the interaction with the amino group(s) of A (see inset in Figure 4). This configuration, that can be considered as representative of this kind of situations, allows to minimize steric hindrance and to fit almost perfectly the A residue between the three silanol groups, as witnessed by the geometrical parameters of the newly formed $-\mathrm{SiO_3}$ fragment (Si−O bonds lengths in the range 1.65–1.67 Å and O−Si−O bond angles in

the range 107-110°), which resulted essentially equivalent to those of the same fragment in other part of the pristine surface.

[Figure 4 about here.]

Despite the reactions of Hal−Si(6,3)$^{3-}$ with both APTES and AEAPTMS release a small quantity of energy (ΔE = -15.0 and -43.3 kJ mol^{-1}, respectively), the global reactions energies, which are calculated starting from pristine halloysite nanotubes and by taking into account the formation energy (-1395.4 kJ mol^{-1}) of Hal−Si(6,3)$^{3-}$, are -1410.4 kJ mol^{-1} for A = APTES and -1438.8 kJ mol^{-1} for A = AEAPTMS. Then, these reactions are thermodynamically the most favored among those investigated, in agreement with the high availability of Si−OH active sites on the surface of the nanoclay model and the disappearance of the ring tensions which affected some of the previous structures.

At this point of the discussion it is worth to note that, due to the lacking of cooperativity characterizing the formation of silanol groups (Ferrante et al., 2023), the most favourable situation is the one where a large number of functionalization reactions take place through a single hydrolsys process, like (2) and (6), localized in regions of the outer Hal surface which are distant from each other. Reactions like (9) would occur istead when silanol groups are clustered on the surface, which could happen after the treatment at high alkaline conditions. It is to say that this last arrangement would be auspicable, since it could lead to the realization of a surface with a high concentration of functionalization, hence a high density of anchoring point, useful, for example, to stabilize metal nanoparticles.

Literature also reports that, as an extremization of the alkaline treatment, the breaking of a fourth Si−O bond can be caused together with the extraction of orthosilicic acid, $Si(OH)_4$, from the surface of halloysite. The corresponding reaction is reported below:

$$\mathrm{Hal} + 3\,\mathrm{H_2O} + \mathrm{OH^-} \longrightarrow \mathrm{Hal{-}Si{-}v_1{}^-} + \mathrm{Si(OH)_4} \tag{10}$$

where the silicic surface presents a vacancy surrounded by OH groups. Since this property can be important for the functionalization of Hal with organosilanes,

whose alkoxysilyl moieties could be incorporated in the surface, the following reactions were simulated:

$$\mathrm{Hal{-}Si{-}v_1}^{-} + \mathrm{A} \longrightarrow \mathrm{Hal{-}S^vA^0} + 3\,\mathrm{ROH} \tag{11}$$

In this case, the nucleophilic attack is carried out from three OH left at the center of the vacancy, after the extraction of the orthosilicic acid. The optimized structures of the $\mathrm{Hal{-}S^vA^0}$ species are reported in Figure 5.

[Figure 5 about here.]

Reactions (11) occur with an energy consumption of 53.0 and 58.9 $\mathrm{kJ\,mol^{-1}}$ for A=APTES and AEAPTMS, respectively. The reactions global energies, calculated from pristine halloysite nanotubes and taking into account the formation of the $\mathrm{Hal{-}Si{-}v_1}^{-}$ species (-650.4 $\mathrm{kJ\,mol^{-1}}$) are -597.4 and -591.5 $\mathrm{kJ\,mol^{-1}}$, respectively. It is clear that these reactions are less thermodynamically favored than the functionalizations on silicic surfaces bearing silicon-based tetrahedra before any extraction of orthosilicic acid occurred. In the $\mathrm{Hal{-}S^vA^0}$ structures, the silicon atom from A, substituting the one lost as $\mathrm{Si(OH)_4}$, is not equivalent to the other Si centers on the surface. As a matter of fact, none of these last could form bonds with any molecule protruding outwards, since their $\mathrm{SiO_3}$ tetrahedra have a cavity facing up and the fourth Si−O bond is formed with the interlayer; conversely, the Si originating from A shows the $\mathrm{SiO_3}$ tetrahedron with the cavity facing downwards and is located just above the interlayer oxygen atom bearing the negative charge, at a distance of 2.84 Å from it. Consequently, the three Si−O−Si bond angles that realize on the edge of the functionalization cannot have the typical value of 132° which characterize the other centers on the surface, but their values (166° on the average) witness a much linear arrangement. Likely for these reasons reactions (11) are endothermic.

Finally, the functionalization of halloysite inner lumen was also studied by simulating the product of the following reactions, which would occur on the untreated aluminum-based surface:

$$\mathrm{Hal} + \mathrm{A} \longrightarrow \mathrm{Hal{-}Al{-}A^0} + 3\,\mathrm{ROH} \tag{12}$$

The two organosilanes react with three OH groups of the inner surface of halloysite, resulting in its silanization. The optimized structures are reported in Figure 6. It is to be noted that the silicon atom from A fits almost naturally on the AlO hexagonal arrangement, with Si−O bond lengths equal to 1.68 Å on the average, *i.e.* only 0.04 Å longer than the usual; further, the oxygen atoms that coordinate the functionalization only sligthly deviate from their bridged position among two Al centers, showing a closure of 6° of the Al−O−Al angle caused by an averaged Al−O bond elongation of 0.05 Å. In the case of APTES functionalization a H_2N···HO hydrogen bond is formed with the aluminic surface, while AEAPTMS prefers to maintain its intramolecular H-bond.

[Figure 6 about here.]

Both reactions (12) occur with a small release of energy, being ΔE = -99.9 $kJ\,mol^{-1}$ for A = APTES and -61.3 $kJ\,mol^{-1}$ for A = AEAPTMS (which is lower that the APTES case due to the absence of hydrogen bonds with the surface), and there is, in alkaline environment, no other reaction with which they could couple. By comparing these values with the reaction energies characterizing the functionalizations occurring at the outer silicic surface, it is possible to assess that the attachment of both APTES and AEAPTMS is preferred on the modified Si external array. It is worth to note, however, that in the aluminum surface the functionalization with APTES and AEAPTMS could occur directly on the pristine Hal, without pretreatment.

4.2. Experimental study of the functionalization efficiency

The section on the computational investigations above report the results about the selective functionalization of halloysite silicic surface, which exploit the formation of active sites with hydroxyl groups, as a consequence of the alkaline hydrolysis. It was showed that the silanization with 3-aminopropyltriethoxysilane (APTES) and N-3-(trimethoxysilyl)propyl-ethylenediamine (AEAPTMS) of the pretreated nanoclay is a thermodynamically favored reaction which allows one to infer high efficiency. These aspects were investigated experimentally. Thermogravimetric curves for untreated and treated Hal modified with APTES and

AEAPTMS are reported in Figure 7, whereas the thermogravimetric parameters are reported in Table 3.

[Figure 7 about here.]

[Table 3 about here.]

As it can be observed, the mass residues at 800 °C of all the functionalized samples are lower than the final mass of pristine Hal and aHal (see Figure S7 of Supporting Information). Since the organic matter undergoes thermal degradation in this range of temperature, the mass residue at 800 °C is decreasing with increasing the amount of organic counterpart in each sample. Therefore, it can be assessed that the functionalization with the organosilanes occurred. Moreover, MR_{800} for aHal-APTES and aHal-AEAPTMS are lower than the values for Hal-APTES and Hal-AEAPTMS. These findings are related to a more efficient grafting on the surface of the nanotubes after the treatment with the base. In order to provide a more detailed evaluation of the grafting efficiency, the loading of APTES on both Hal-APTES and aHal-APTES was calculated and it resulted to be 9.5 and 10.9 wt%, respectively. Similarly, the grafting efficiency was calculated to be 8.6 and 11.0 wt% for Hal-AEAPTMS and aHal-AEAPTMS. As a consequence, the treatment of halloysite with sodium hydroxide effectively improved the functionalization of its surface. Experimental evidences are in good agreement with the computational results.

The attachment of the organosilane molecules onto halloysite was also investigated by FTIR spectroscopy. Figure 8 reports the spectra of Hal and alkaline pretreated Hal before and after functionalization with APTES, as an example (see Figure S8 of Supporting Information for the AEAPTMS case). It is worth to observe that the positions of the typical bands of halloysite at 3695 and 3620 cm^{-1} are not affected by the grafting. Since these two bands are related to the OH-stretching vibrations of the Al_2OH groups inside the lumen (Lisuzzo et al., 2020b), any interactions arising between the aluminols groups and the organic molecules could be disregarded. Most importantly, after the silanization is car-

ried out, some new bands appear in the 1800-1200 cm^{-1} range (magnifications in Figure 8).

[Figure 8 about here.]

The deformation (scissoring) of NH_2 at 1561/1571 cm^{-1}, the deformation (scissoring) of CH_2 at 1490/1494 cm^{-1}, the deformation (wagging) of CH_2 at 1385/1387 cm^{-1} and the deformation (scissoring) of Si−CH at 1335/1339 cm^{-1} can be clearly identified in the spectra of both Hal-APTES and aHal-APTES. Also, APTES-modified samples exhibit some new FTIR peaks at around 2930 cm^{-1}, related to the CH_2 stretching vibration. These results confirm that the functionalization was achieved (Yuan et al., 2008b).

Aimed at quantitatively evaluating the silanization of the the nanoclays, XRF experiments were carried out and the Si/Al ratios for the samples before and after the APTES and AEAPTMS functionalization were measured (result reported in Table 4).

[Table 4 about here.]

It is clear that the Si/Al ratio increases due to the functionalization with the organosilanes, which brings more Si atoms on the surface of the nanotubes. It is worth to note that, in agreement with thermogravimetric data, the increase is higher for aHal-APTES compared to Hal-APTES, and for aHal-AEAPTMS compared to Hal-AEAPTMS. These results represent a further proof that the functionalization of halloysite surface with the organisilanes is improved after the alkaline pretreatment of the nanoclay with sodium hydroxide.

Finally, X-Ray Diffraction analysis was conducted in order to evaluate any possible variations on the structure of halloysite nanotubes. Diffractograms are reported in Figure 9.

[Figure 9 about here.]

The pattern of pristine Hal shows the typical reflections at 2θ = 12.0, 20.4 and 24.5° corresponding to the (001) basal spacing of 0.73 nm, (020)/(110) basal

spacing of 0.44 nm and (002) basal spacing of 0.35 nm, respectively (Barot et al., 2020). The presence of the first peak, which depends on the distance between the different layers of the nanotubes, indicates that the clay is in the 7Å-form and it is consequently dehydrated. After the treatment with NaOH and the functionalization with both APTES and AEAPTMS, the reflections are not displaced. This finding confirms that no intercalation occurred and that the functionalization of halloysite was carried out maintaining its morphological properties and its peculiar hollow nanotubular shape, in agreement with the literature (Ferrante et al., 2023).

5. Conclusions

In this work, a computational investigation based on density functional theory is conducted in order to have detailed atomistic insights about both the structural properties of halloysite nanotubes functionalized with organosilanes and also on the energetics of the reactions involved. It was found that the alkaline activation of the nanoclay, by pretreatment with a base, has deep effects on the grafting of organic molecules. Computational results suggested that the interaction with halloysite outer surface is thermodynamically favored when the nanotubes display silanols groups, which act as active sites for the nucleophilic attack on the silicon center of the organosilanes. In particular, the breaking of three Si−O bonds in three different Si centers of the silicic array provided the best conditions (i.e. number of active sites and high configurational flexibility) for the reaction with APTES and AEAPTMS, being the global process energies -1410.4 and -1438.8 $kJ\,mol^{-1}$, respectively. Moreover, this study also showed that the functionalization of the inner aluminum based surface of halloysite is less favored, by a thermodynamic point of view, being the calculated reaction energies -99.9 and -61.3 $kJ\,mol^{-1}$ for APTES and AEAPTMS attachment on the internal lumen. Aimed at supporting the computational findings, experimental analysis were also carried out. Thermogravimetry showed that the functionalization efficiency improved after the alkaline pretreatment of Hal, reaching the

highest values of 10.9 and 11.0 wt% for aHal-APTES and aHal-AEAPTMS. The successful functionalization was confirmed by FTIR spectroscopy, which allowed to identify the appearance of new bands typical of the organisilanes on the spectra of the functionalized materials. X-Ray Fluorescence analysis furtherly proved that the amount of silicon atoms on halloysite surface increased after the functionalization and, in particular, at a higher extent for the alkali activated clay compared to the pristine Hal. Finally, XRD measurements showed that the grafting did not alter the morphological properties of halloysite nanotubes, whose hollow nanotubular shape is preserved without any intercalation in the interlayer space. On the whole, these results prove that the functionalization of halloysite is enhanced as a consequence of the alkaline pretreatment and due to the creation of silanol active groups on the surface. Since the chemical modification of halloysite surface is very often the first step before its use in any technological application, this work opens up new perspectives about the optimization of reactions and processes where aluminosilicates are involved, especially in catalysis.

Acknowledgements

Funding are gratefully acknowlegded by "SiciliAn MicronanOTecH Research And innovation CEnter - SAMOTHRACE" (MUR, PNRR-M4C2, ECS_0000002), spoke 3, Università degli Studi di Palermo, "S2-COMMs-Micro and Nanotechnologies for Smart & Sustainable Communities". LL thanks the European Union for co-financing within the FESR e FSE, PON "Ricerca e Innovazione 2014-2020 - DM 1062/2021"

References

Barot, T., Rawtani, D., & Kulkarni, P. (2020). Physicochemical and biological assessment of silver nanoparticles immobilized halloysite nanotubes-based resin composite for dental applications. *Heliyon*, *6*, e03601. doi:https://doi.org/10.1016/j.heliyon.2020.e03601.

Blanco, I., Cicala, G., Latteri, A., Saccullo, G., El-Sabbagh, A. M. M., & Ziegmann, G. (147-153). Thermal characterization of a series of lignin-based polypropylene blends. *Journal of Thermal Analysis and Calorimetry*, *127*, 2017. doi:https://doi.org/10.1007/s10973-016-5596-2.

Cataldo, S., Lazzara, G., Massaro, M., Muratore, N., Pettignano, A., & Riela, S. (2018). Functionalized halloysite nanotubes for enhanced removal of lead(ii) ions from aqueous solutions. *Appl. Clay Sci.*, *156*, 87–95. doi:https://doi.org/10.1016/j.clay.2018.01.028.

De Silva, R. T., Pasbakhsh, P., Lee, S. M., & Kit, A. Y. (2015). Zno deposited/encapsulated halloysite–poly(lactic acid) (PLA) nanocomposites for high performance packaging films with improved mechanical and antimicrobial properties. *Applied Clay Science*, *111*, 10–20. doi:https://doi.org/10.1016/j.clay.2015.03.024.

Eichkorn, K., Weigend, F., Treutler, O., & Ahlrichs, R. (1997). Auxiliary basis sets for main row atoms and transition metals and their use to approximate coulomb potentials. *Theor. Chem. Acc.*, *97*, 119–124. doi:https://doi.org/10.1007/s002140050244.

Ferrante, F., Armata, N., Cavallaro, G., & Lazzara, G. (2017). Adsorption studies of molecules on the halloysite surfaces: A computational and experimental investigation. *J Phys. Chem. C*, *121*, 2951–2958. doi:https://doi.org/10.1021/acs.jpcc.6b12876.

Ferrante, F., Armata, N., & Lazzara, G. (2015). Modeling of the halloysite spiral nanotube. *J Phys. Chem. C*, *119*, 16700–16707. doi:https://doi.org/10.1021/acs.jpcc.5b04281.

Ferrante, F., Bertini, M., Ferlito, C., Lisuzzo, L., Lazzara, G., & Duca, D. (2023). A computational and experimental investigation of halloysite silicic surface modifications after alkaline treatment. *Appl. Clay Sci.*, *232*, 106813. doi:https://doi.org/10.1016/j.clay.2022.106813.

Frisch, M. J., Trucks, G. W., Schlegel, H. B., Scuseria, G. E., Robb, M. A., Cheeseman, J. R., Scalmani, G., Barone, V., Petersson, G. A., Nakatsuji, H., Li, X., Caricato, M., Marenich, A. V., Bloino, J., Janesko, B. G., Gomperts, R., Mennucci, B., Hratchian, H. P., Ortiz, J. V., Izmaylov, A. F., Sonnenberg, J. L., Williams-Young, D., Ding, F., Lipparini, F., Egidi, F., Goings, J., Peng, B., Petrone, A., Henderson, T., Ranasinghe, D., Zakrzewski, V. G., Gao, J., Rega, N., Zheng, G., Liang, W., Hada, M., Ehara, M., Toyota, K., Fukuda, R., Hasegawa, J., Ishida, M., Nakajima, T., Honda, Y., Kitao, O., Nakai, H., Vreven, T., Throssell, K., Montgomery, J. A., Jr., Peralta, J. E., Ogliaro, F., Bearpark, M. J., Heyd, J. J., Brothers, E. N., Kudin, K. N., Staroverov, V. N., Keith, T. A., Kobayashi, R., Normand, J., Raghavachari, K., Rendell, A. P., Burant, J. C., Iyengar, S. S., Tomasi, J., Cossi, M., Millam, J. M., Klene, M., Adamo, C., Cammi, R., Ochterski, J. W., Martin, R. L., Morokuma, K., Farkas, O., Foresman, J. B., & Fox, D. J. (2016). Gaussian 16 Revision C.01.

Haw, T. T., Hart, F., Rashidi, A., & Pasbakhsh, P. (2020). Sustainable cementitious composites reinforced with metakaolin and halloysite nanotubes for construction and building applications. *Appl. Clay Sci.*, *188*, 105533. doi:https://doi.org/10.1016/j.clay.2020.105533.

Hua, Y., Guo, T., Li, F., Fu, L., & Yang, H. (2023). The structure evolution of halloysite nanotubes during the acid leaching process: A molecular dynamics study. *Appl. Clay. Sci.*, *242*, 107021. doi:https://doi.org/10.1016/j.clay.2023.107021.

Kryuchkova, M., Danilushkina, A., Lvov, Y., & Fakhrullin, R. (2016). Evaluation of toxicity of nanoclays and graphene oxide in vivo: A paramecium caudatum study. *Environ. Sci.*, *3*, 442–452. doi:https://doi.org/10.1039/C5EN00201J.

Lisuzzo, L., Cavallaro, G., Milioto, S., & Lazzara, G. (2020a). Effects of halloysite content on the thermo-mechanical performances

of composite bioplastics. *Applied Clay Science*, *185*, 105416. doi:https://doi.org/10.1016/j.clay.2019.105416.

Lisuzzo, L., Cavallaro, G., Milioto, S., & Lazzara, G. (2022). Halloysite nanotubes as nanoreactors for heterogeneous micellar catalysis. *J. Colloid Interface Sci.*, *608*, 424–434. doi:https://doi.org/10.1016/j.jcis.2021.09.146.

Lisuzzo, L., Cavallaro, G., Parisi, F., Milioto, S., & Lazzara, G. (2019). Colloidal stability of halloysite clay nanotubes. *Ceramics International*, *45*, 2858–2865. doi:https://doi.org/10.1016/j.ceramint.2018.07.289.

Lisuzzo, L., Wicklein, B., Dico, G. L., Lazzara, G., Real, G. d., Aranda, P., & Ruiz-Hitzky, E. (2020b). Functional biohybrid materials based on halloysite, sepiolite and cellulose nanofibers for health applications. *Dalton Trans.*, *49*, 3830–3840. doi:https://doi.org/10.1039/C9DT03804C.

Liu, M., Chang, Y., Yang, J., You, Y., He, R., Chen, T., & Zhou, C. (2016). Functionalized halloysite nanotube by chitosan grafting for drug delivery of curcumin to achieve enhanced anticancer efficacy. *J. Mater. Chem. B*, *4*, 2253–2263. doi:https://doi.org/10.1039/C5TB02725J.

Liu, M., Fakhrullin, R., Novikov, A., Panchal, A., & Lvov, Y. (2019). Tubule nanoclay-organic heterostructures for biomedical applications. *Macromol. Biosci.*, *19*, 1800419. doi:https://doi.org/10.1002/mabi.201800419.

Liu, T., Zhang, J., Ouyang, P., Fu, L., & Yang, H. (2021). The relation between nanotube diameter, length and surface area and pore volume of multiwalled spiral halloysite nanotubes: A theoretical study. *Appl. Clay. Sci.*, *215*, 106303. doi:https://doi.org/10.1016/j.clay.2021.106303.

Lvov, Y., Wang, W., Zhang, L., & Fakhrullin, R. (2016). Halloysite clay nanotubes for loading and sustained release of functional compounds. *Advanced Materials*, *28*, 1227–1250. doi:https://doi.org/10.1002/adma.201502341.

Makó, E., Dódony, I., Pekker, P., Pósfai, M., Kovács, A., Ható, Z., & Kristóf, T. (2020). Nanoscale structural and morphologi-

cal features of kaolinite nanoscrolls. *Appl. Clay Sci.*, *198*, 105800. doi:https://doi.org/10.1016/j.clay.2020.105800.

Massaro, M., Licandro, E., Cauteruccio, S., Lazzara, G., Liotta, L. F., Notarbartolo, M., Raymo, F. M., Sánchez-Espejo, R., Viseras-Iborra, C., & Riela, S. (2022). Nanocarrier based on halloysite and fluorescent probe for intracellular delivery of peptide nucleic acids. *J. Colloid Interface Sci.*, *620*, 221–233. doi:https://doi.org/10.1016/j.jcis.2022.03.151.

Mehdizadeh, M., Sadjadi, S., Poater, A., Mansouri, A., & Bahri-Laleh, N. (2022). Molecular modelling aided catalyst design for pao oils hydrofinishing. *J. Mol. Liq.*, *352*, 118675. doi:https://doi.org/10.1016/j.molliq.2022.118675.

Panchal, A., Rahman, N., Konnova, S., Fakhrullin, R., Zhang, D., Blake, D., John, V., Ivanov, E., & Lvov, Y. (2020). Clay nanotube liquid marbles enhanced with inner biofilm formation for the encapsulation and storage of bacteria at room temperature. *ACS Appl. Nano Mater.*, *3*, 1263–1271. doi:https://doi.org/10.1021/acsanm.9b02033.

Pasbakhsh, P., Churchman, G. J., & Keeling, J. L. (2013). Characterisation of properties of various halloysites relevant to their use as nanotubes and microfibre fillers. *Applied Clay Science*, *74*, 47–57. doi:https://doi.org/10.1016/j.clay.2012.06.014.

Rozhina, E., Batasheva, S., Miftakhova, R., Yan, X., Vikulina, A., Volodkin, D., & Fakhrullin, R. (2021). Comparative cytotoxicity of kaolinite, halloysite, multiwalled carbon nanotubes and graphene oxide. *Appl. Clay Sci.*, *205*, 106041. doi:https://doi.org/10.1016/j.clay.2021.106041.

Sadjadi, S., & Atai, M. (2018). Ternary hybrid system of halloysite nanotubes, polyacrylamides and cyclodextrin: An efficient support for immobilization of pd nanoparticles for catalyzing coupling reaction. *Appl. Clay Sci.*, *153*, 78–89. doi:https://doi.org/10.1016/j.clay.2017.12.013.

Sadjadi, S., Hosseinnejad, T., Malmir, M., & Heravi, M. M. (2017). Cu@furfural imine-decorated halloysite as an efficient heterogeneous catalyst for promoting ultrasonic-assisted a3 and ka2 coupling reactions: A combination of experimental and computational study. *New J. Chem.*, *41*, 13935–13951. doi:https://doi.org/10.1039/C7NJ02272G.

Schaefer, A., Horn, H., & Ahlrichs, R. (1992). Fully optimized contracted gaussian-basis sets for atoms li to kr. *J. Chem. Phys.*, *97*, 2571–2577. doi:https://doi.org/10.1063/1.463096.

Shankar, S., Kasapis, S., & Rhim, J.-W. (2018). Alginate-based nanocomposite films reinforced with halloysite nanotubes functionalized by alkali treatment and zinc oxide nanoparticles. *International Journal of Biological Macromolecules*, *118*, 1824–1832. doi:https://doi.org/10.1016/j.ijbiomac.2018.07.026.

Sidorenko, A. Y., Kravtsova, A. V., Aho, A., Heinmaa, I., Volcho, K. P., Salakhutdinov, N. F., Agabekov, V. E., & Murzin, D. Y. (2018). Acid-modified halloysite nanotubes as a stereoselective catalyst for synthesis of 2H-chromene derivatives by the reaction of isopulegol with aldehydes. *ChemCatChem*, *10*, 3950–3954. doi:https://doi.org/10.1002/cctc.201800974.

Sidorenko, A. Y., Kurban, Y. M., Aho, A., Ihnatovich, Z. V., Kuznetsova, T. F., Heinmaa, I., Murzin, D. Y., & Agabekov, V. E. (2021). Solvent-free synthesis of tetrahydropyran alcohols over acid-modified clays. *mol. Catal.*, *499*, 111306. doi:https://doi.org/10.1016/j.mcat.2020.111306.

Spepi, A., Duce, C., Pedone, A., Presti, D., Rivera, J.-G., Ierardi, V., & Tiné, M. R. (2016). Experimental and DFT characterization of halloysite nanotubes loaded with salicylic acid. *J. Phys. Chem. C*, *120*, 26759–26769. doi:https://doi.org/10.1021/acs.jpcc.6b06964.

Takahara, Y. K., Ikeda, S., Ishino, S., Tachi, K., Ikeue, K., Sakata, T., Hasegawa, T., Mori, H., Matsumura, M., & Ohtani, B. (2005). Asym-

metrically modified silica particles: A simple particulate surfactant for stabilization of oil droplets in water. *J. Am. Chem. Soc.*, *127*, 6271–6275. doi:https://doi.org/10.1021/ja043581r.

Vergaro, V., Lvov, Y. M., & Leporatti, S. (2012). Halloysite clay nanotubes for resveratrol delivery to cancer cells. *Macromol. Biosci.*, *12*, 1265–1271. doi:https://doi.org/10.1002/mabi.201200121.

Wang, Q., Zhang, J., & Wang, A. (2013). Alkali activation of halloysite for adsorption and release of ofloxacin. *Appl. Surf. Sci.*, *287*, 54–61. doi:https://doi.org/10.1016/j.apsusc.2013.09.057.

Yuan, P., Southon, P. D., Liu, Z., Green, M. E. R., Hook, J. M., Antill, S. J., & Kepert, C. J. (2008a). Functionalization of halloysite clay nanotubes by grafting with γ-aminopropyltriethoxysilane. *J. Phys. Chem. C*, *112*, 15742–15751. doi:https://doi.org/10.1021/jp805657t.

Yuan, P., Southon, P. D., Liu, Z., Green, M. E. R., Hook, J. M., Antill, S. J., & Kepert, C. J. (2008b). Functionalization of halloysite clay nanotubes by grafting with γ-aminopropyltriethoxysilane. *J. Phys. Chem. C*, *112*, 15742–15751. doi:https://doi.org/10.1021/jp805657t.

Zhang, H., Cheng, C., Song, H., Bai, L., Cheng, Y., Ba, X., & Wu, Y. (2019a). A facile one-step grafting of polyphosphonium onto halloysite nanotubes initiated by Ce(IV). *Chem. Commun.*, *55*, 1040–1043. doi:http://dx.doi.org/10.1039/C8CC08667B.

Zhang, Y., Bai, L., Cheng, C., Zhou, Q., Zhang, Z., Wu, Y., & Zhang, H. (2019b). A novel surface modification method upon halloysite nanotubes: A desirable cross-linking agent to construct hydrogels. *Appl. Clay Sci.*, *182*, 105259–105267. doi:https://doi.org/10.1016/j.clay.2019.105259.

Zhao, Y., & Truhlar, D. G. (2006). A new local density functional for main-group thermochemistry, transition metal bonding, thermochemical

kinetics, and noncovalent interactions. *J. Chem. Phys.*, *125*, 194101. doi:https://doi.org/10.1063/1.2370993.

Zhu, K., Duan, Y., Wang, F., Gao, P., Jia, H., Ma, C., & Wang, C. (2017). Silane-modified halloysite/Fe_3O_4 nanocomposites: Simultaneous removal of Cr(VI) and Sb(V) and positive effects of Cr(VI) on Sb(V) adsorption. *Chem. Eng. J.*, *311*, 236–246. doi:https://doi.org/10.1016/j.cej.2016.11.101.

Zsirka, B., Horváth, E., Szabó, P., Juzsakova, T., Szilágyi, R. K., Fertig, D., Makó, E., Varga, T., Kónya, Z., Kukovecz, A., & Kristóf, J. (2017). Thin-walled nanoscrolls by multi-step intercalation from tubular halloysite-10å and its rearrangement upon peroxide treatment. *Appl. Surf. Sci.*, *399*, 245–254. doi:https://doi.org/10.1016/j.apsusc.2016.12.053.

List of Figures

1 The (3-aminopropyl)triethoxysilane (APTES) and the N-3-(trimethoxysilyl)propyl ethylenediamine (AEAPTMS) molecules. 28

2 The DFT optimized geometries of the Hal−S^1A^2 system, with A = APTES (a) and A = AEAPTMS (b), representing the product of process (2). For the sake of visualization, only the functionalized silicic portion of the model is shown in the main picture, while the whole molecular model is reported in stick representation in the upper corner. Color code: H-pink, C-grey, N-blue, O-red, Si-green. Hydrogen bonds are represented by dashed lines. 29

3 The DFT optimized geometries of the Hal−S^2A^1 system, with A = APTES (a) and A = AEAPTMS (b), representing the product of process (6). For the sake of visualization, only the functionalized silicic portion of the model is shown in the main picture, while the whole molecular model is reported in stick representation in the upper corner. Color code: H-pink, C-grey, N-blue, O-red, Si-green. Hydrogen bonds are represented by dashed lines. 30

4 The DFT optimized geometries of the Hal−S^3A^0 system, with A = APTES (a) and A = AEAPTMS (b), representing the product of process (9). For the sake of visualization, only the functionalized silicic portion of the model is shown in the main picture, while the whole molecular model is reported in stick representation in the upper corner. Color code: H-pink, C-grey, N-blue, O-red, Si-green. Hydrogen bonds are represented by dashed lines. The peculiar SiO configuration is depicted in the inset, with the Si originating from the functionalization evidenced in red. 31

5 The DFT optimized geometries of the Hal−S^vA^0 system, with A = APTES (a) and A = AEAPTMS (b), representing the product of process (11). For the sake of visualization, only a portion of the functionalized silicic surface is shown. Color code: H-pink, C-grey, N-blue, O-red, Si-green. 32

6 The DFT optimized geometries of the Hal−Al−A^0 system, with A = APTES (a) and A = AEAPTMS (b), representing the product of process (12). For the sake of visualization, only a portion of the functionalized aluminic surface is shown. Color code: H-pink, C-grey, N-blue, O-red, Al-cyan. In the case of APTES the picture is enlarged to allow appreciating the details of the anchoring configuration. 33

7 Thermogravimetric curves of APTES and AEAPTMS functionalized Hal and alkaline pretreated Hal. 34

8 FTIR spectra of Hal and alkaline pretreated Hal before and after functionalization with APTES. 35

9 Diffractograms of Hal, aHal, Hal-APTES, aHal-APTES, Hal-AEAPTMS and aHal-AEAPTMS. 36

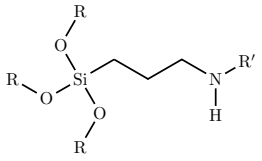

APTES: R′=H R=Et
AEAPTMS: R′=$(CH_2)_2NH_2$ R=Me

Figure 1: The (3-aminopropyl)triethoxysilane (APTES) and the N-3-(trimethoxysilyl)propyl ethylenediamine (AEAPTMS) molecules.

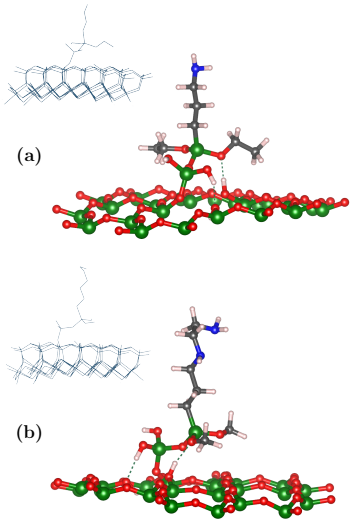

Figure 2: The DFT optimized geometries of the Hal−S^{1}A^2 system, with A = APTES (a) and A = AEAPTMS (b), representing the product of process (2). For the sake of visualization, only the functionalized silicic portion of the model is shown in the main picture, while the whole molecular model is reported in stick representation in the upper corner. Color code: H-pink, C-grey, N-blue, O-red, Si-green. Hydrogen bonds are represented by dashed lines.

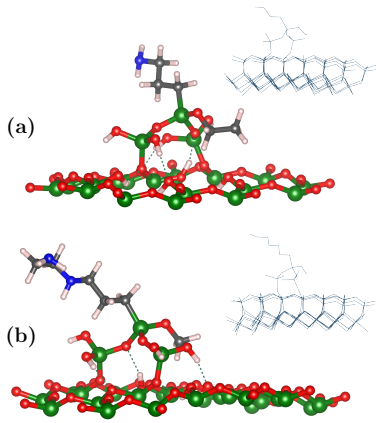

Figure 3: The DFT optimized geometries of the Hal−S^2A^1 system, with A = APTES (a) and A = AEAPTMS (b), representing the product of process (6). For the sake of visualization, only the functionalized silicic portion of the model is shown in the main picture, while the whole molecular model is reported in stick representation in the upper corner. Color code: H-pink, C-grey, N-blue, O-red, Si-green. Hydrogen bonds are represented by dashed lines.

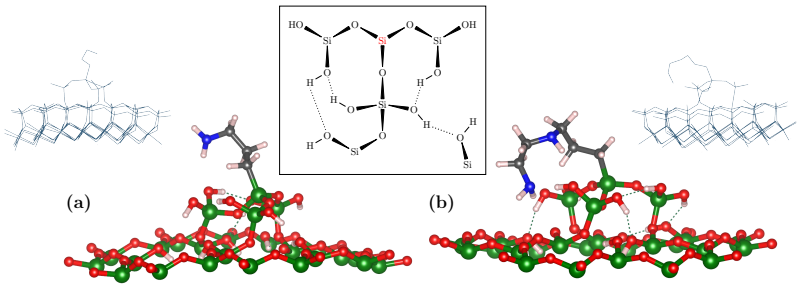

Figure 4: The DFT optimized geometries of the Hal−S^3A^0 system, with A = APTES (a) and A = AEAPTMS (b), representing the product of process (9). For the sake of visualization, only the functionalized silicic portion of the model is shown in the main picture, while the whole molecular model is reported in stick representation in the upper corner. Color code: H-pink, C-grey, N-blue, O-red, Si-green. Hydrogen bonds are represented by dashed lines. The peculiar SiO configuration is depicted in the inset, with the Si originating from the functionalization evidenced in red.

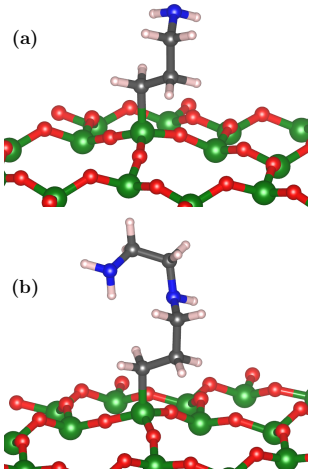

Figure 5: The DFT optimized geometries of the Hal−S^vA^0 system, with A = APTES (a) and A = AEAPTMS (b), representing the product of process (11). For the sake of visualization, only a portion of the functionalized silicic surface is shown. Color code: H-pink, C-grey, N-blue, O-red, Si-green.

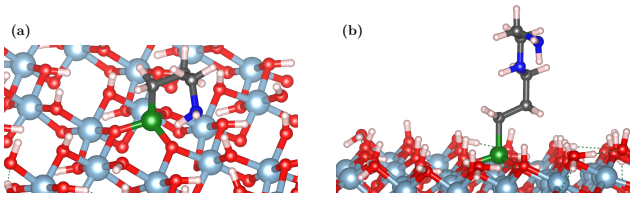

Figure 6: The DFT optimized geometries of the Hal−Al−A^0 system, with A = APTES (a) and A = AEAPTMS (b), representing the product of process (12). For the sake of visualization, only a portion of the functionalized aluminic surface is shown. Color code: H-pink, C-grey, N-blue, O-red, Al-cyan. In the case of APTES the picture is enlarged to allow appreciating the details of the anchoring configuration.

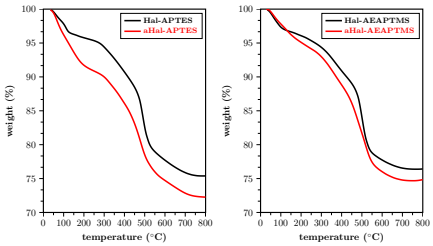

Figure 7: Thermogravimetric curves of APTES and AEAPTMS functionalized Hal and alkaline pretreated Hal.

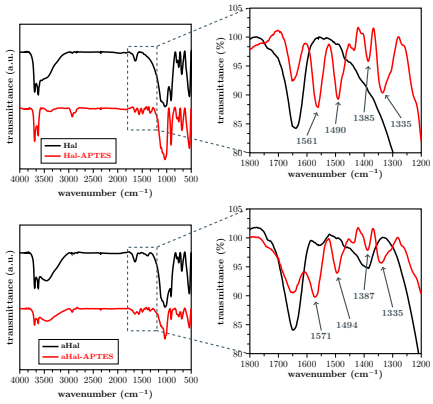

Figure 8: FTIR spectra of Hal and alkaline pretreated Hal before and after functionalization with APTES.

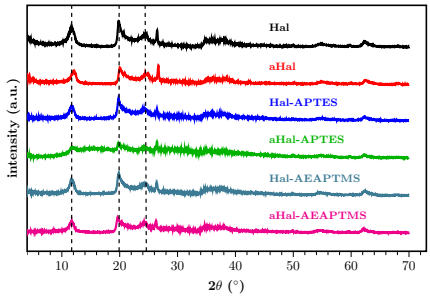

Figure 9: Diffractograms of Hal, aHal, Hal-APTES, aHal-APTES, Hal-AEAPTMS and aHal-AEAPTMS.

List of Tables

1 Global energies (ΔE) for all the investigated functionalization reactions. R = Et for APTES, R = Me for AEAPTMS. 38
2 Reaction energies for the Hal$-$Si(2 m,m)$^{m-}$+A $\longrightarrow$ Hal$-$S^{m}A^{3-n}+ nROH functionalization. 39
3 Thermogravimetric parameters (wt%) of pristine Hal and alkaline pretreated Hal functionalized with APTES and AEAPTMS. . . . 40
4 Si/Al ratios for Hal and alkaline pretreated Hal before and after functionalization with APTES and AEAPTMS. 41

Table 1: Global energies (ΔE) for all the investigated functionalization reactions. R = Et for APTES, R = Me for AEAPTMS.

reaction	$\Delta E/kJ\,mol^{-1}$	
	A=APTES	A=AEAPTMS
$Hal + 2\,H_2O + OH^- + A \longrightarrow Hal{-}S^1A^2 + ROH$	-727.5	-714,4
$Hal + 2\,H_2O + OH^- + A \longrightarrow Hal{-}S^1A^1 + 2\,ROH$	-732.5	-719.9
$Hal + 2\,H_2O + OH^- + A \longrightarrow Hal{-}S^1A^0 + 3\,ROH$	-509.3	-507.8
$Hal + 4\,H_2O + 2\,OH^- + A \longrightarrow Hal{-}S^2A^1 + 2\,ROH$	-1125.8	-1130.7
$Hal + 4\,H_2O + 2\,OH^- + A \longrightarrow Hal{-}S^2A^0 + 3\,ROH$	-972.5	-964.3
$Hal + 6\,H_2O + 3\,OH^- + A \longrightarrow Hal{-}S^3A^0 + 3\,ROH$	-1410.4	-1438.8
$Hal + 3\,H_2O + OH^- + A \longrightarrow Hal{-}S^vA^0 + Si(OH)_4 + 3\,ROH$	-587.4	-591.5
$Hal + A \longrightarrow Hal{-}Al{-}A^0 + 3\,ROH$	-99.9	-61.3

Table 2: Reaction energies for the Hal−Si(2 m,m)$^{m-}$ + A ⟶ Hal−S^{m}A^{3-n} + nROH functionalization.

	Reaction energy/kJ mol^{-1}					
	A = APTES			A = AEAPTMS		
	n			n		
m	1	2	3	1	2	3
1	-31.0	-36.0	187.2	-17.9	-23.4	188.8
2		-6.0	147.3		-11.0	155.4
3			-15.0			-43.3

Table 3: Thermogravimetric parameters (wt%) of pristine Hal and alkaline pretreated Hal functionalized with APTES and AEAPTMS.

Sample	$\mathbf{ML_{150}}$	$\mathbf{MR_{800}}$	$\mathbf{MD_{800}}$
Hal[a]	2.2	83.8	10.0
aHal[a]	3.4	83.4	13.2
Hal-APTES	3.7	75.3	21.0
aHal-APTES	6.3	72.3	21.4
Hal-AEAPTMS	3.3	76.4	20.2
aHal-AEAPTMS	3.8	74.8	21.5

[a] See (Ferrante et al., 2023)

Table 4: Si/Al ratios for Hal and alkaline pretreated Hal before and after functionalization with APTES and AEAPTMS.

Sample	**Si/Al ratio**
Hal	1.28[a]
aHal	1.27[a]
Hal-APTES	1.49
aHal-APTES	1.58
Hal-AEAPTMS	1.43
aHal-AEAPTMS	1.65

[a] See (Ferrante et al., 2023)